MATERIALS SCIENCE

Three-dimensional shrinking electronics on freestanding and freeform curvilinear surfaces

Yangbo Yuan[1], Dongliang Chen[2], Jianyu Li[2], Bowen Li[1,3], Abu Musa Abdullah[1,4], Fatema Tuz Zohra[1], Wanqing Zhang[1], Xianzhe Zhang[1], Xin Xin[1], Mohammad Ali Amidian[1], Ankan Dutta[5,6], Feifei Shi[2]*, Huanyu Cheng[1]*

Wearable electronics that adapt to three-dimensional (3D) surfaces are essential for next-generation smart internet of things (IoT), yet existing strategies remain limited because of fabrication complexity, material incompatibility, or poor structural control. Here, this work introduces a scalable yet versatile approach to design and fabricate 3D electronic systems by printing liquid metal patterns onto heat-shrinkable polymer substrates. Upon controlled thermal actuation, the 2D circuits transform into target 3D geometries with enhanced electrical performance. The resulting 3D shrinking electronics enable conformal antenna integration for IoT devices and gesture-interactive wearable interfaces. This low-cost, versatile platform offers a paradigm for customizable, shape-adaptive electronics in intelligent real and virtual environments.

INTRODUCTION

With the continuous advancement of electronic manufacturing technologies, conventional two-dimensional (2D) electronic devices are gradually evolving into 3D systems with more complex architectures and higher functional integration (*1*, *2*). Compared to traditional 2D electronics, 3D electronic systems offer improved spatial efficiency by enabling vertical stacking of components and better utilization of limited space (*3*). They also provide greater design customizability, allowing devices to be tailored in shape, size, and layout to conform to irregular surfaces or confined spaces (*4*). These advantages highlight the vast application potential and commercial value of 3D electronics in emerging fields such as wearable technology, the smart internet of Things (IoT), and human-machine interfaces (HMIs).

In recent years, extensive research efforts have been dedicated to the development of 3D electronics. One representative approach involves the fabrication of flexible and hybrid flexible electronic devices, which can conform to complex and even surfaces for wearable and biomedical applications (*5*–*10*). In addition, several studies have explored the integration of liquid metal (LM) with flexible substrates to enhance stretchability and electrical conductivity upon large tensile strains for improved conformability in the deformable electronic systems. These systems leverage the fluidic nature and excellent conductivity of LMs to maintain electrical performance under extreme mechanical deformation. Such designs have been successfully implemented in diverse applications, including health monitoring (*11*, *12*), motion tracking (*13*), HMI (*14*), and soft robotics (*15*, *16*). However, these technologies are inherently planar in nature, focusing primarily on conformability and mechanical compliance, and thus, fall short in constructing truly 3D electronic architectures.

Another class of strategies centers on the direct fabrication of circuits on target surfaces by 3D printing (*17*–*19*), laser direct writing (*20*, *21*), in situ growth (*22*), or transfer printing (*23*, *24*). While these methods offer high structural design freedom and spatial control of functional materials for creating multilayered structures and personalized devices, they still face challenges such as the need for specialized equipment and/or complex fabrication processes. These limitations hinder their scalability and cost-effectiveness in producing high-resolution, large-area 3D electronics.

A variety of strategies and materials have been developed to transform planar structures into complex 3D forms, including origami-inspired folding (*25*, *26*), mechanical buckling (*27*), and thermoplastic reshaping (*28*). Among them, thermoforming exploits the softened state of thermoplastic materials after heating, allowing them to deform with external force and further conform onto complex 3D surface or structures. This approach is cost-effective and suitable for high-throughput manufacturing, which has been widely explored in packaging (*29*) and structural electronic encapsulations (*30*). However, the deformation of most thermoplastics in thermoforming is irreversible and mold-dependent, making the final geometry entirely dictated by predesigned molds and presenting challenges for use that requires customization or reconfigurability.

In summary, there remains a critical need for an efficient, low-cost, and shape-controllable method to fabricate conformable 3D electronics on varying target freeform surfaces. In response to this challenge, this work integrates thermally shrinkable polymer sheets with LM to construct 3D shrinking electronics. Specifically, 2D LM-based circuit patterns are first printed onto thermally shrinkable substrates, followed by a controlled thermal shrinkage process that transforms the flat circuits onto targeted 3D configurations. Compared to metallic conductors with similar electrical performance (*31*–*33*), LM uniquely retains excellent morphological integrity and even achieves higher electrical conductivity during substrate shrinking without forming wrinkles or cracks (*34*, *35*). In contrast to other flowable conductive materials such as silver ink (*36*) and hydrogels (*37*–*39*), LM offers higher electrical conductivity (table S1). The printability and adhesion of LM on the polymer surface are further enhanced by encapsulating and dispersing LM droplets with sodium dodecylbenzenesulfonate (SDBS) via ultrasonication, resulting in an SDBS-encapsulated LM

[1]Department of Engineering Science and Mechanics, The Pennsylvania State University, University Park, PA 16802, USA. [2]John and Willie Leone Family Department of Energy and Mineral Engineering, The Pennsylvania State University, University Park, PA 16802, USA. [3]School of Science, Engineering, and Technology, The Pennsylvania State University, Harrisburg, 777 W Harrisburg Pike, Middletown, PA 17057, USA. [4]Department of Mechanical Engineering and Mechanics, Drexel University, Philadelphia, PA 19104, USA. [5]Department of Mechanical Engineering, The Pennsylvania State University, University Park, PA 16803, USA. [6]Center for Neural Engineering, The Pennsylvania State University, University Park, PA 16802, USA.
*Corresponding author. Email: feifeishi@psu.edu (F.S.); huanyu.cheng@psu.edu (H.C.)

composite (SLM). Combined with surface plasma treatment, photothermal folding, and strategic pattern design, the versatile toolbox reported in this work enables the design and conformal integration of antennas on various 3D surfaces for smart IoT applications. Moreover, a smart 3D shrinking ring with an embedded miniaturized accelerometer provides the proof-of-concept system-level demonstration for gesture-based HMI control, highlighting the potential of this technique for smart, wearable 3D devices. The reported framework, with low manufacturing cost, broad material compatibility, and precise structural control, provides a promising route toward the next-generation 3D electronic device systems.

RESULTS

Fabrication of 3D shrinking electronics

Patterning LM on prestretched polystyrene (PPS) sheets followed by thermally induced shrinkage offers a simple yet effective route for fabricating 3D electronic architectures. However, the weak interfacial adhesion between pristine LM and the PPS may lead to relative displacement or flow during the shrinking process, compromising circuit integrity and functional reliability. Efforts to address this issue have led to the use of the surfactant SDBS to modify the LM surface for rendering hydrophilicity (*40*, *41*). Specifically, SDBS and LM ultrasonically allow the hydrophobic alkyl tails of SDBS to approach LM, while the hydrophilic sulfonate groups remain exposed on the surface, forming a surfactant-coated hydrophilic LM composite. Hydrophilic functional groups such as carboxyl and hydroxyl groups in the PPS introduced by plasma treatment can then form hydrogen bonds with the SLM during the printing process, enhancing interfacial adhesion and minimizing delamination or failure during thermal shrinkage (Fig. 1A). Moreover, the SLM composite generated through ultrasonic dispersion and drying exhibits a biphasic structure composed of both solid and liquid components, thereby offering improved mechanical stability compared to pristine LM (*42*, *43*).

Upon completion of the patterning process, heating the sample triggers the release of residue stress within the PPS. The stretching-induced alignment of polymer chains during PPS film formation can allow these chains to recover their energetically favorable, disordered coil state upon heating (*44*–*46*), leading to rapid macroscopic contraction or shrinking along the prestressed directions (Fig. 1B). By leveraging this process, prepatterned 2D electronic circuits can be transformed into geometrically defined 3D structures with increased pattern spatial resolution and enhanced electrical conductivity, enabling the fabrication of arbitrarily shaped 3D electronic systems with excellent structural compatibility and functional versatility. This simple yet versatile approach provides a route to fabricate 3D wearable devices for HMI (Fig. 1C) and 3D conformal antennas for smart IoT applications (Fig. 1D).

Characterization of SLM

Varying the mass ratio of SDBS to LM determines the optimal value. While different amounts of SDBS have negligible influence on the electrical conductivity of the resulting SLM (fig. S1), the increased SDBS content increases the proportion of solid phase in the SLM to eventually lead to severe particle agglomeration when the mass ratio reaches 3.5%. Therefore, a mass ratio of 2.0% is selected for subsequent experiments unless specified otherwise.

The advantages of SLM over pristine LM in terms of adhesion and mechanical stability are first verified in the contact angle measurements in an argon atmosphere (to avoid the interference of LM surface oxidation). Before plasma treatment of the PPS (fig. S2), both LM and SLM exhibit contact angles of greater than 120°, indicating a hydrophobic nature. After plasma treatment, the contact angle of LM slightly decreases but is still larger than 120°, whereas that of SLM drops below 90° (Fig. 2A) to exhibit a hydrophilic behavior. This result confirms that ultrasonic mixing with SDBS introduces hydrophilic groups on the SLM surface, leading to enhanced wettability on hydrophilic substrates.

The adhesion between LM/SLM and the substrate is further assessed with mechanical pull-off tests. An identical plasma-treated PPS mounted on the bottom surface of a force sensor is brought into contact with LM or SLM, followed by pull-off to measure the adhesion force. The results reveal that the SLM exhibits 20% stronger adhesion to PPS than LM for both before and after thermal shrinkage, attributed to hydrogen bonding between the hydrophilic SLM and PPS substrate. Moreover, the SLM/PPS adhesion further increases from 0.0355 N/cm^2 before shrinkage to 0.0517 N/cm^2 by 45.6% after shrinkage (Fig. 2B), which can be ascribed to the increased contact area due to the formation of a porous surface morphology on the PPS sheet after shrinkage (Fig. 2D and fig. S3). The stronger interfacial adhesion between uniformly coated SLM and plasma-treated PPS can also provide a much more stable conductive pathway even upon moderate mechanical friction (fig. S4 and movie S1). According to Pouillet's law $\left(R/R_0 = (1+\varepsilon)^2\right)$ for incompressible materials, where R is the resistance, R_0 is the initial resistance, and ε is the strain, the normalized resistance changes of SLM as a function of tensile strain are much smaller than those of GaIn and biphasic GaIn (bGaIn) (Fig. 2C), indicating excellent mechanical stability of SLM. Moreover, cyclic tensile testing at 100% strain demonstrates the stable resistance response of SLM over repeated stretching and release cycles compared with GaIn and bGaIn (fig. S5), further confirming its mechanical robustness. Scanning electron microscopy (SEM) images of the surface morphology reveal that SLM contains a higher proportion of solid-phase structures compared to GaIn (Fig. 2E and fig. S6), which contributes to enhanced mechanical stability (*42*, *43*).

Elemental analysis using energy-dispersive x-ray spectroscopy (EDS) further confirms the successful incorporation of SDBS. Compared to LM only with signals from Ga, In, and O (fig. S7), SLM also features signals from C and Na elements (Fig. 2F), indicating the effective wrapping of LM by SDBS. It is worth noting that the electron beam may also change the phase of GaIn; thus, a more accurate and quantitative measurement may be required to confirm the result. There are no distinct peaks in the x-ray diffraction (XRD) pattern of the SLM, suggesting the absence of crystalline phases (Fig. 2G). Raman spectroscopy results also reveal multiple Raman shifts in SLM (Fig. 2H) attributed to the presence of SDBS, in contrast to the single peak observed in LM (*47*, *48*).

Ultrasonic treatment effectively disperses LM into particles, primarily due to cavitation effects occurring near the interface and within the bulk liquid phase (*49*). The introduction of SDBS as a surfactant further facilitates control over the particle diameter and enhances the stability of the dispersion (*50*, *51*). Compared with LM prepared by a single ultrasonic process, the SLM obtained after a second round of ultrasonication following SDBS addition features a

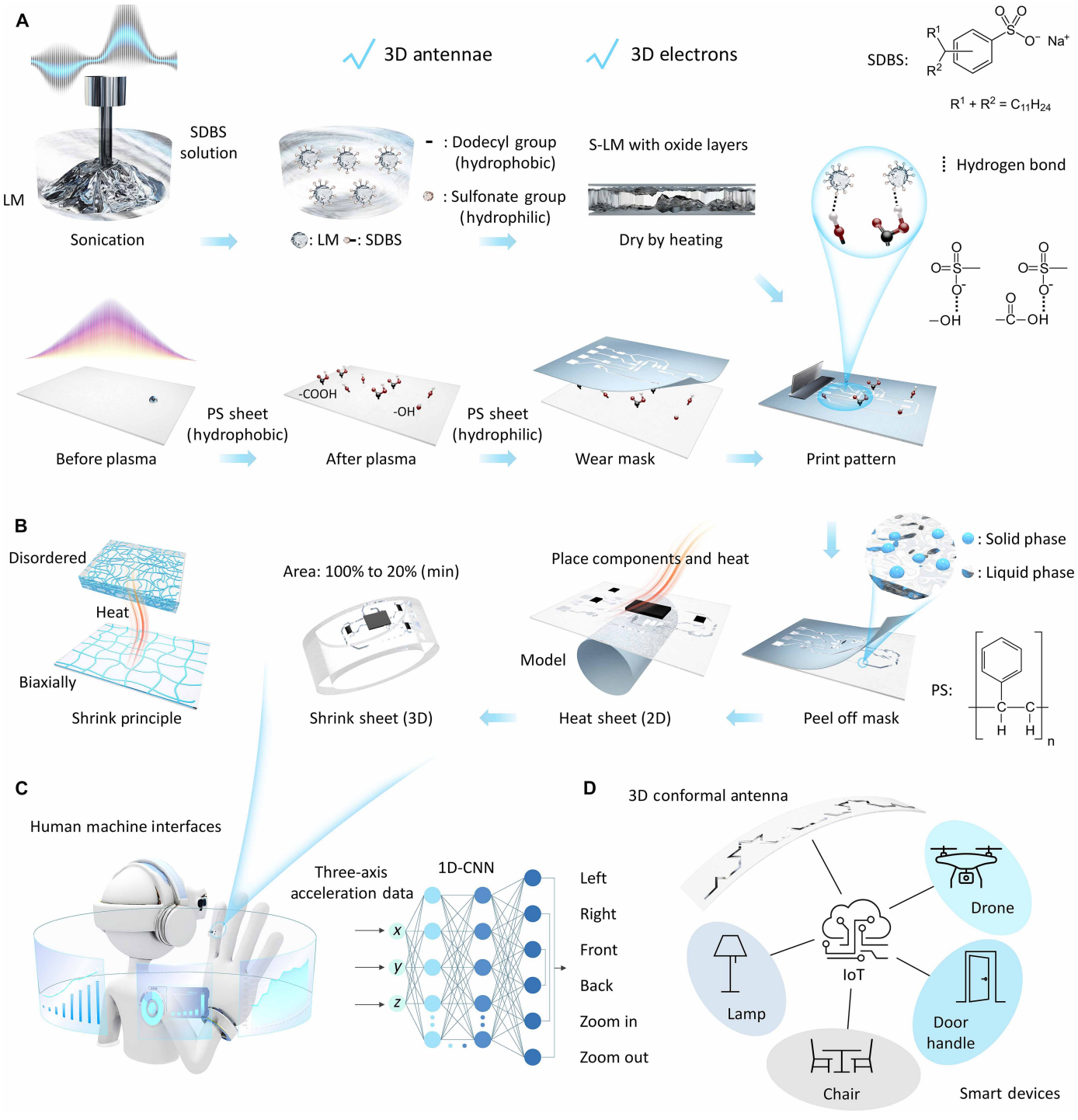

Fig. 1. Fabrication process and application scenarios of 3D shrinking electronics. (**A**) Schematic showing the fabrication process for 3D shrinking electronics. Liquid metal (LM) is ultrasonically dispersed in a sodium dodecylbenzenesulfonate (SDBS) solution to form SDBS-wrapped LM (SLM). After drying, the SLM is printed onto a thermally shrinkable plasma-treated prestretched polystyrene (PPS) sheet covered by a patterned polyimide (PI) shadow mask, where hydrogen bonding enhances interfacial adhesion. After peeling off the shadow mask and placing the patterned PPS sheet onto a 3D object, heating the PPS sheet induces volumetric shrinkage to transform the 2D planar circuit into a conformal 3D electronic structure with integrated components. (**B**) Schematic showing the thermal shrinking mechanism of the PPS sheet. (**C**) The 2D electronics are shrunk into a smart wearable ring with an integrated miniaturized accelerometer, enabling human-machine interaction through gesture recognition based on three-axis acceleration data processed by a 1D convolutional neural network (1D-CNN). (**D**) 2D planar antennas shrunk onto the surfaces of drones, door handles, lamps, and chairs form 3D conformal antennas, enabling smart internet of things (IoT).

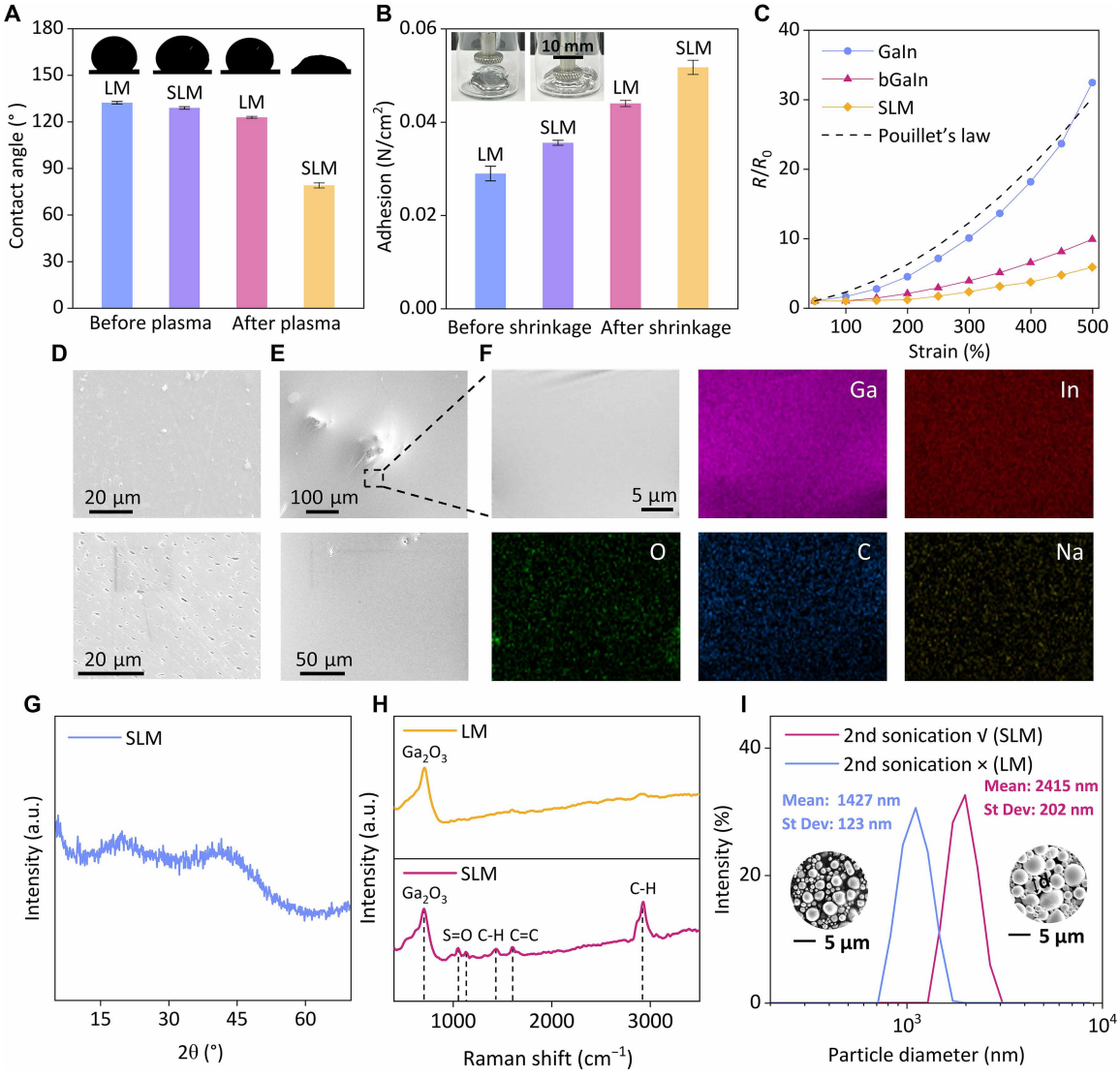

Fig. 2. Characterizations of interfacial, structural, and electrical properties of LM and SLM. (**A**) Contact angles of LM and SLM on PPS surfaces before and after plasma treatment. (**B**) Adhesion strength of LM and SLM on PPS surfaces measured before and after shrinkage. (**C**) Normalized resistance (R/R_0) of GaIn, bGaIn, and SLM as a function of applied tensile strain, along with a reference curve based on Pouillet's law. (**D**) Scanning electron microscopy (SEM) images of the PPS surface before (top) and after (bottom) shrinkage. (**E**) SEM images of SLM (top) and LM (bottom). (**F**) Energy-dispersive x-ray spectroscopy (EDS) mapping of the SLM. (**G**) X-ray diffraction (XRD) of the SLM. (**H**) Raman spectra of LM and SLM. (**I**) Particle size distribution of LM and SLM, with corresponding SEM images shown in the insets.

larger average particle diameter (Fig. 2I and fig. S8) and a more uniform dispersion (fig. S9).

Electrical and geometric characterization

During the thermal shrinking of the PPS, the overlying SLM patterns also undergo deformation due to the interfacial forces. Evaluation of the essential electrical performance, such as resistance changes of SLM with different linewidths after shrinking, shows an improvement in conductivity (Fig. 3A). Both the linewidth and line length L of SLM decrease during the shrinking process (Fig. 3B) to affect the resistance. As the SLM is nearly incompressible (*52*) with the total amount remaining as almost constant, the initially planar SLM traces transform into dome-like structures after shrinking (Fig. 3, C and D, and fig. S10).

Control over the resulting 3D geometry of the shrinking electronic structures can be achieved by designing the printed patterns of black ink as localized absorbers of near-infrared (NIR) light. Upon NIR exposure, the ink locally heats the underlying PPS, raising its temperature above the glass transition temperature (T_g). This induces localized stress relaxation and causes anisotropic shrinking perpendicular to the ink lines, thereby triggering self-folding behavior. In other words, the black ink lines act as actuation hinges, guiding the folding direction by controlling the ink placement, and determining the folding angle through the width of the ink pattern, light intensity, and exposure time (Fig. 3E). When the entire structure or sheet is heated above T_g, the folded 3D structure can further shrink to approximately 20% of its original planar area (*53*), with the thickness increased to about 600% of its original value. This uniform

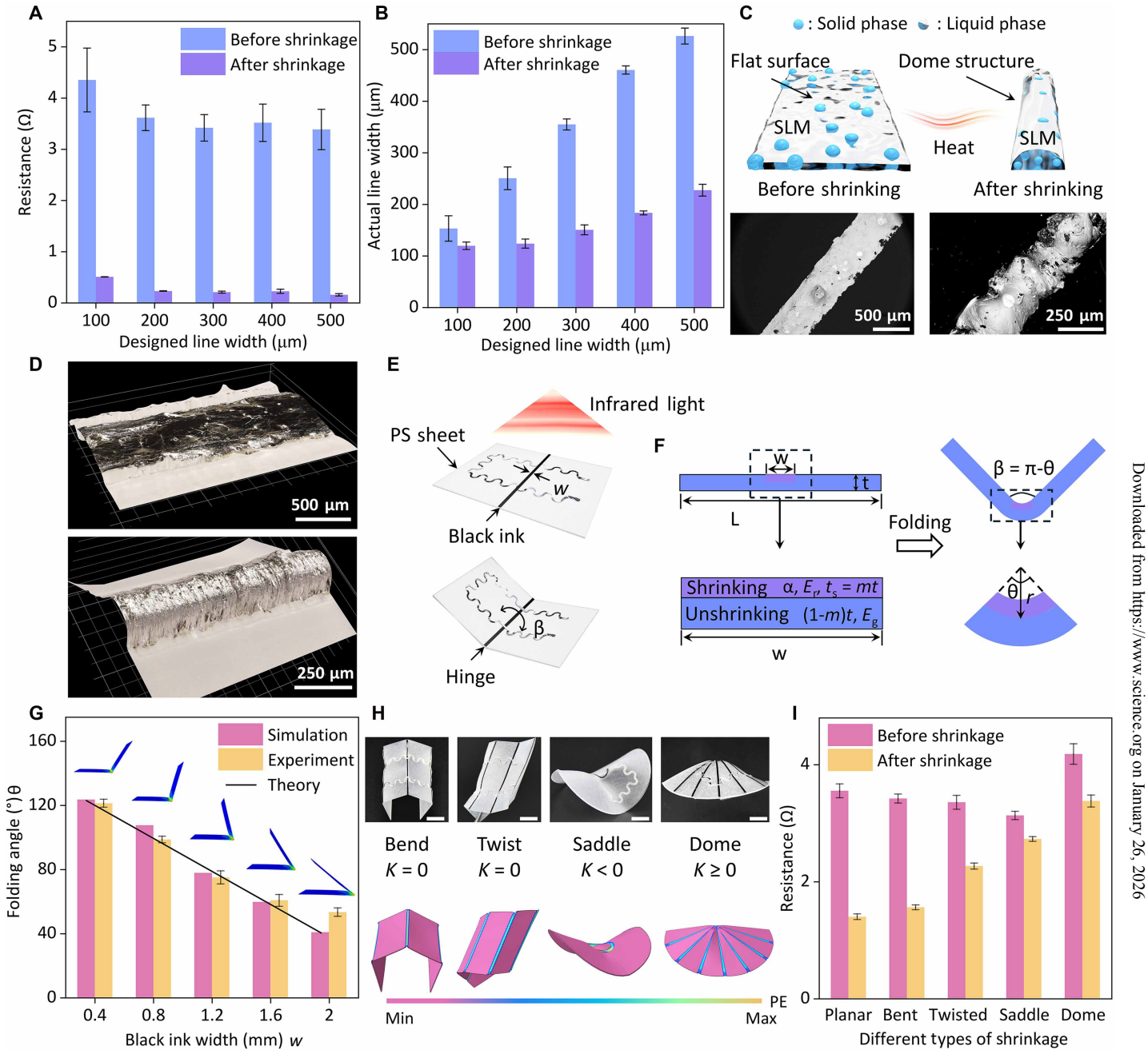

Fig. 3. Conductivity and geometry characterizations of 3D shrinking electronics from uniform or localized remote heating. (**A**) Resistance changes of SLM lines with different widths before and after shrinkage. (**B**) Measured line widths of SLM before and after shrinkage. (**C**) Schematic and SEM images showing the surface morphology changes of SLM before and after shrinkage. (**D**) 3D optical images of SLM line before (top) and after (bottom) shrinkage. (**E**) Schematic showing the localized folding about the black ink line triggered by NIR absorption, along with (**F**) geometric definition of folding angle and hinge width in the localized shrinking region. (**G**) Folding angle (θ) as a function of black ink width (*w*) from simulation, experiment, and theory. (**H**) Comparison between experiment (top) and simulation (bottom) of different 3D shapes after shrinking, bending, twisting, saddle, and dome structures. (**I**) Resistance changes of SLM traces on different 3D shapes/structures before and after shrinkage.

and predictable shrinkage behavior is also experimentally observed in PPS samples with different geometries (e.g., rectangle, equilateral triangle, and circle). The measured changes in planar dimensions and thickness before and after shrinkage confirm the reproducibility of the shrinkage ratio (fig. S11 and table S2).

To quantitatively investigate the relationship between the folding angle β and the ink line width *w*, a simplified bilayer beam model is established (Fig. 3F), where the composite beam has a total thickness of *t* and a length of *L*. The printed ink area with a width *w* and a thickness $t_s = mt$ (*m* as the thickness ratio) serves as the shrinking layer (purple) with a thermal coefficient of expansion $\alpha < 0$ on top of the unshrunk layer (blue). Both materials are assumed to be isotropic and linearly elastic. The Young's modulus of the material in its rubbery (E_r) and glassy (E_g) states captures the stiffness variation

upon heating. When a temperature gradient ΔT is applied between the two regions, the bending angle θ can be expressed as $\theta = w/r$, where r is the bending radius given as

$$\frac{1}{r} = \frac{-6\alpha\Delta T}{t\left[4+2m^2-2m+\frac{m^3 n}{1-m}+\frac{(1-m)^3}{mn}\right]}$$

with $n = E_r/E_g$. The folding angle β is then obtained as $\beta = \pi - \theta = \beta = \pi - \theta = \pi - w/r$ (fig. S12), which is linear proportional to both the ink line width w and the thermal mismatch (or shrinking) strain $\varepsilon_r = -\alpha\Delta T$.

The theoretical predictions of this model are validated by finite element simulations of the self-folded bilayer composite film, with thermal input upon NIR irradiation simulated by temperature increase. As the ink linewidth w increases from 0.4 to 2.0 mm (with other parameters unchanged), the folding angle measured in the experiment decreases from 121° to 53°, which also agrees with both the theoretical predictions and simulated results (Fig. 3G and fig. S13). Without having to use the more complicated thickness variations as in the previous literature (*54*), the controlled folding modulated by the ink line width can be exploited for origami-inspired construction of varying 3D structures upon remote NIR trigger. These structures with zero, positive, or negative Gaussian curvatures can be programmed to fold into desired shapes through judicially designed predefined ink patterns (Fig. 3H and fig. S14), as confirmed by both simulation (movie S2) and experimental results (movie S3). Notably, the resistance of the SLM traces decreases after shrinking for all these 3D geometries (Fig. 3I). Compared with the complete shrinkage in Fig. 3A, the decrease in conductor length is relatively smaller, resulting in a less pronounced reduction in resistance according to the resistance calculation ($R = \rho L/A$). Beyond freestanding programmed folding structures, this technique can also be used to conform the shrinking electronics onto freeform target 3D shapes such as a golf ball, when heated with a hot-air gun (fig. S15). Further combining origami (*55*, *56*) strategies and kirigami-inspired cuts (*57*–*59*) or even Gaussian conformal designs (*60*) can result in enhanced conformability on complex 3D surfaces.

3D conformal antenna

In smart home environments, transforming everyday objects into intelligent devices for smart IoTs hinges on the use of the essential component to wirelessly communicate with each other. Radio-frequency antennas play a critical role in wireless communication, but the diverse geometries of household items make it prohibitively expensive to design customized antennas for each individual object. A promising alternative is to use thermally induced shrinking to conform antennas onto objects with varying shapes, thereby reducing manufacturing costs.

Nevertheless, antenna performance is highly sensitive to geometric alterations (*61*, *62*). Since the shrinking process inherently changes antenna dimensions, maintaining desirable antenna performance under such large deformations presents a major challenge. Benefiting from the self-similarity of fractal structures, fractal dipole antennas are adopted in this work (fig. S16) to maintain their performance across different frequency bands even after isotropic scaling (*63*).

Despite the large shrinking, PPS exhibits uniform and predictable shrinkage behavior (fig. S17), making it suitable for designing antenna structures with tunable sizes and geometries. For example, the appropriate preshrinking antenna size and frequency response can be designed with the help of coupled mechanics-electromagnetics simulation, such that the postshrinking antenna naturally tunes to the desired target operating frequency of 2.5 GHz (Fig. 4, A and B). The transformation of the antennas conformed onto the complex 3D surfaces also induces bending and/or twisting, but this impact on the antenna performance changes is minimized by the inherent symmetry of the dipole structure that ensures a uniform current distribution (Fig. 4C) and consistent radiation patterns (Fig. 4, D and E, and fig. S18). Compared to traditional dipole antennas, fractal dipole antennas also demonstrate multiple operational bands (figs. S19 to S22). The total effective electrical length L_n of a Koch fractal antenna increases exponentially with the iteration number n (=2 here), following $L_n = L_0 \cdot (4/3)^n$, where L_0 is the length of a conventional dipole. This extended current path allows for compact physical dimensions while preserving resonance at lower frequencies, making it highly advantageous for multiband and miniaturized antenna applications. By tuning the shrinking ratio of PPS through controlling the heating time and applied external force, antennas operating at additional frequency bands can be further engineered (fig. S23). The experimental results of the antenna before and after thermal shrinking (Fig. 4F and fig. S24) confirm its practical feasibility. Moreover, the antenna retains stable performance under various bending radii from 34.4 to 11.5 cm. (Fig. 4, G and H, and fig. S25), which can be attributed to the symmetrical structure of the fractal dipole and the excellent electromechanical robustness of the SLM upon bending (fig. S26).

The impact of environmental temperature fluctuations and more importantly from the heating during the transformation on the antenna performance needs to be further examined. As the temperature increases from 25° to 50°C, the antenna remains almost unchanged performance and overall functionality (Fig. 4I), with only a slight degradation in S_{11} at elevated temperatures (fig. S27). When thermally shrunk onto common household objects, the antennas continue to exhibit reliable performance (Fig. 4, J and K, and fig. S28). In this context, the shrinkable antenna, together with compatible sensor modules, can be deployed as a plug-in solution to equip conventional daily objects with intelligent wireless capabilities, demonstrating high potential for smart home and IoT applications.

3D shrinking smart ring

The applicability of the reported method also goes beyond the conductive traces to integrated circuits and devices for wearable electronics and HMIs. For instance, the commercial off-the-shelf components, such as a miniaturized accelerometer along with the corresponding signal acquisition circuit (figs. S29 and S30), can be thermally shrunk into a 3D ring form to capture gesture-induced triaxial acceleration signals (fig. S31). The captured signals are transmitted via a microcontroller unit to a host computer (or cloud) and subsequently classified using a 1D convolutional neural network (1D-CNN) for gesture-based HMI (Fig. 5A). The oxide layer on the LM surface from thermal shrinking can impede electrical contact with the electronic components (*64*, *65*). To address this challenge, immersing the electronic components in hydrochloric acid before integration can help remove the surface oxides from the LM traces to ensure a stable electrical connection (fig. S32).

With five human subjects performing six distinct gestures 200 times each, a sizable dataset is constructed for model training and validation. Over 88 training epochs, the network is iteratively optimized, leading

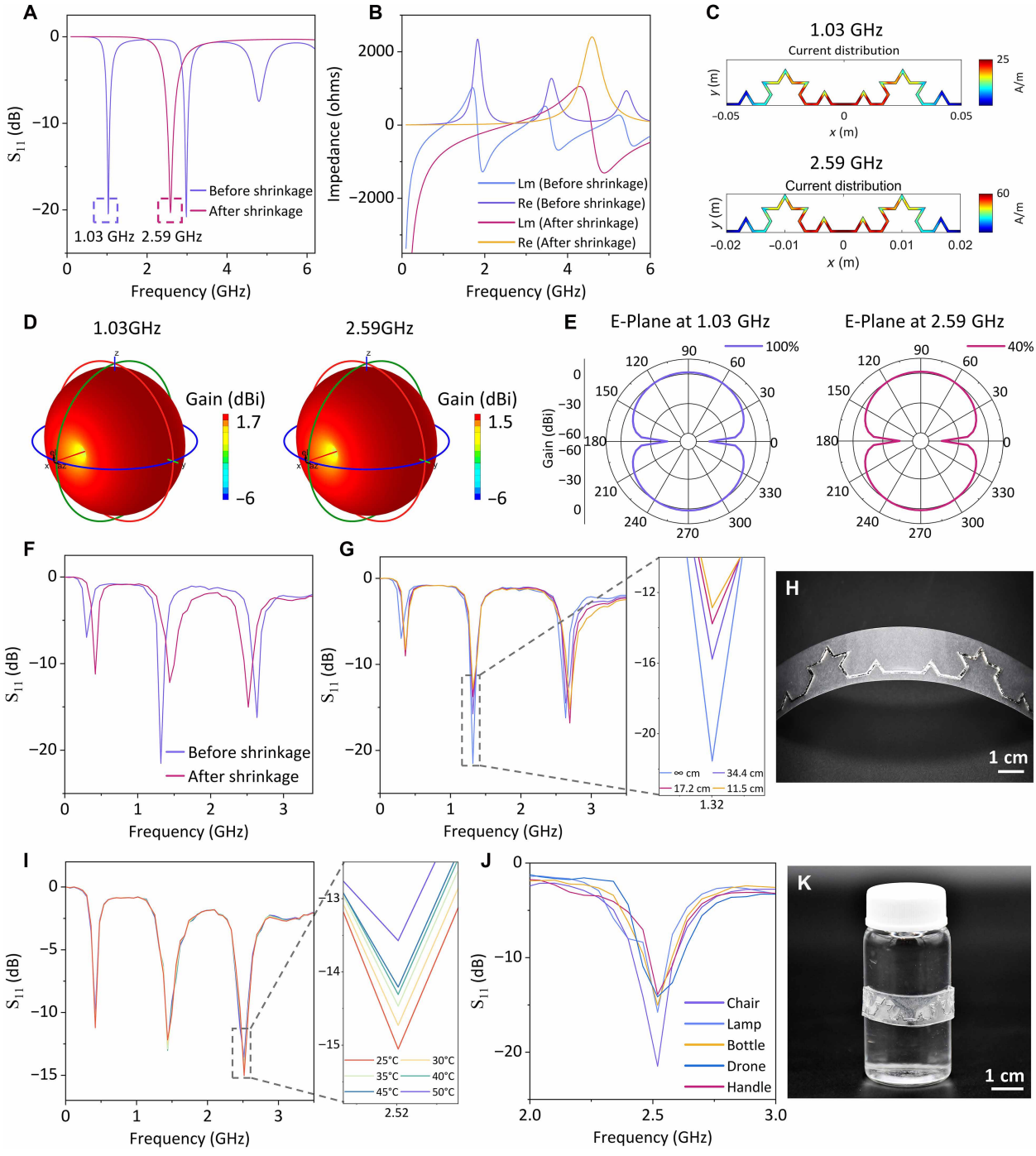

Fig. 4. Simulated and measured radiofrequency (RF) characteristics of the 3D shrinking antenna. Simulated (**A**) reflection coefficients (S_{11}), (**B**) input impedance, (**C**) current distribution at the corresponding resonant frequencies, (**D**) 3D radiation patterns, and (**E**) E-plane radiation patterns of the antenna before and after shrinkage. Measured reflection coefficients of the 3D shrinking antenna (**F**) before and after shrinkage and (**G**) under different bending radii (i.e., ∞, 34.4, 17.2, and 11.5 cm), with a zoomed-in view of the resonant frequency and (**H**) corresponding photograph of the bent antenna. (**I**) Reflection coefficients measured at different temperatures (i.e., 25°, 30°, 35°, 40°, 45°, and 50°C), with a zoomed-in view of the resonant frequency. (**J**) Reflection coefficients of the 3D shrinking antenna conformed to different objects (i.e., chair, lamp, bottle, drone, and handle) with (**K**) corresponding photograph of a bottle-mounted antenna.

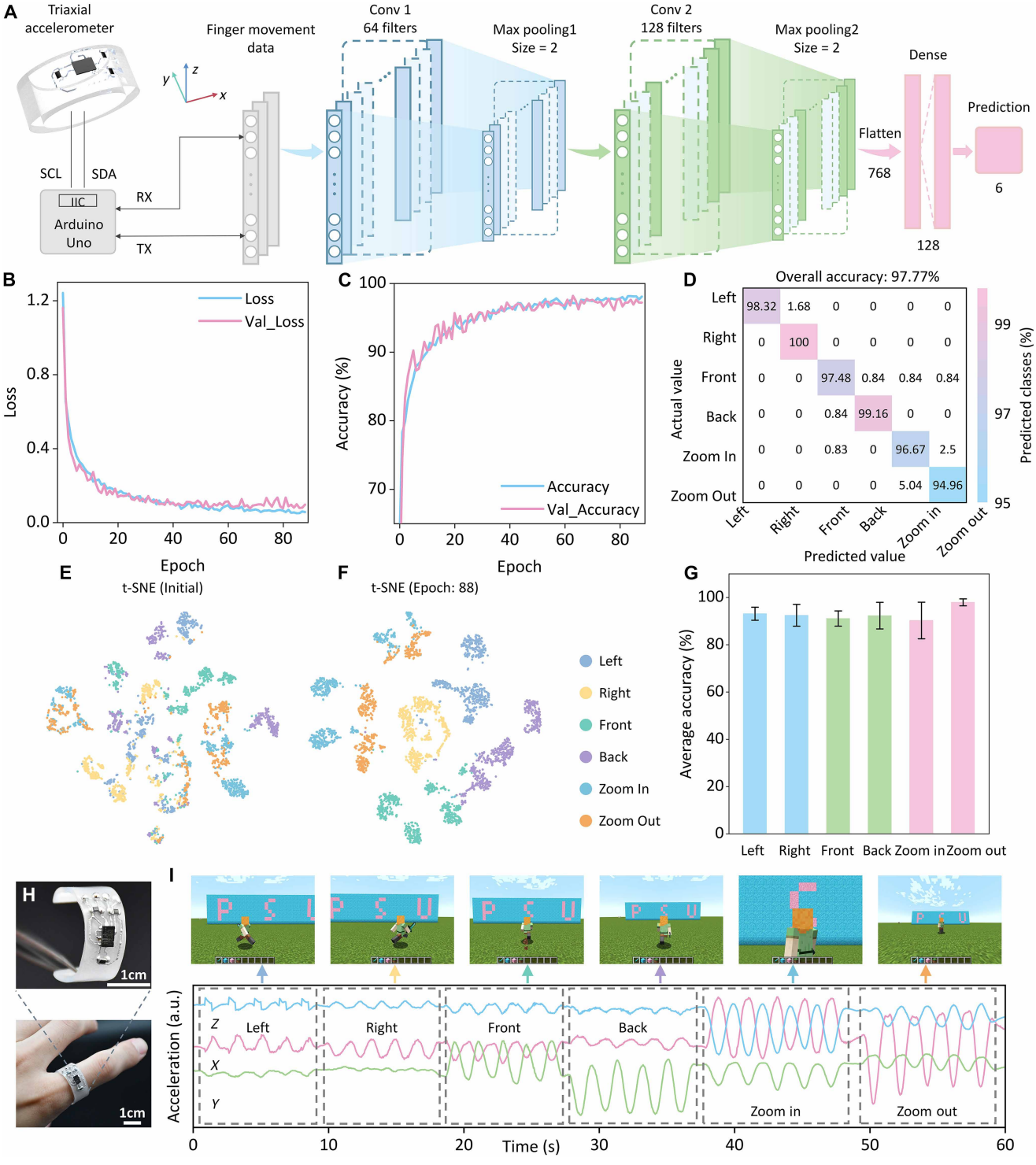

Fig. 5. 3D shrinking smart ring as HMI for gesture recognition. (**A**) Schematic flow diagram of the machine learning algorithm for training and classifying different gestures. (**B**) Loss and (**C**) accuracy rates of the training (blue) and validation (pink) sets over 88 iterations per epochs of the training process. (**D**) Confusion matrix of gesture recognition after 88 iterations. t-SNE visualization of gesture feature distribution (**E**) before training and (**F**) after 88 training epochs. (**G**) Average gesture recognition accuracy on data from three new human subjects using the trained model. (**H**) Photographs of the 3D shrinking smart ring worn on an index finger. (**I**) Gesture-based control of a character in a virtual environment, with corresponding three-axis acceleration signals shown at the bottom.

to progressive reduction in both training and validation losses and a corresponding improvement in classification accuracy (Fig. 5, B and C). Ultimately, the trained model achieves an overall classification accuracy of 97.77%, as illustrated by the confusion matrix (Fig. 5D). The average accuracy of 97.52% from 10 consecutive runs using the same code and dataset (table S3) demonstrates the robustness and high reliability for gesture recognition tasks.

Before neural network training, the data exhibit no discernible pattern in the *t*-distributed stochastic neighbor embedding (t-SNE) projection space (Fig. 5E). However, after 88 training epochs, the clear separations between feature clusters, corresponding to different gestures in the t-SNE visualization (Fig. 5F), confirm the successful feature extraction and discrimination. The model also demonstrates good generalization capability in gesture recognition when tested on data from three new human subjects. Despite the inherent interindividual variability in gesture performance, the model maintains a high classification accuracy with an average of 92.88% on data from three new human subjects (Fig. 5G), indicating its adaptability to user differences.

To further validate the real-world applicability of this gesture recognition system, a custom-built Python-based interface allows for mapping of the classified gesture data to control commands in a computer game environment. This enables intuitive HMI through gesture-based control functions, including directional movement (i.e., left, right, forward, and backward) and perspective zooming in and out (movie S4). The 3D acceleration signals from the 3D shrinking smart ring worn on the index finger (Fig. 5H) generated by different gestures exhibit distinctive signal characteristics (Fig. 5I and movie S5), supporting the high recognition accuracy of the 1D-CNN model.

DISCUSSION

In summary, this study presents a low-cost, efficient, and shape-controllable method to fabricate freestanding and shape-conforming 3D shrinking electronics onto freeform curvilinear surfaces. By patterning SLM on PPS and initiating thermal shrinkage via controlled heating, planar circuit layouts can be transformed into predefined 3D electronic architectures. This method is broadly applicable to the development of emerging class of 3D conformal antennas, enabling stable adhesion to target surfaces while preserving excellent RF performance. It offers advantages in smart IoT systems, including high integration density, geometric design flexibility, and simplified fabrication (*66*–*79*). Furthermore, the reported method also supports the creation of intelligent wearable 3D devices and HMIs, such as the 3D shrinking smart ring for gesture recognition and gaming in the virtual environment. In addition to single-layered circuit layouts, a double-layered design can be realized by laser cutting vias in the PPS sheet before shrinkage, followed by filling the via regions with LM after shrinkage to enable interconnection between the upper and lower circuit layers (fig. S33). Packaging can be achieved via thermoplastic encapsulation using shrinkable thin films such as thermoplastic polyurethane (fig. S34). Combined with the recent developments of augmented reality and virtual reality technologies, the reported manufacturing route along with the corresponding design toolbox can open up opportunities for next-generation smart shape-adaptive electronics for use in both real and virtual environments.

MATERIALS AND METHODS

Preparation of SLM

Gallium (99.99%) and indium (99.995%) were purchased from Luciteria, USA. SDBS was obtained from Sigma-Aldrich (Merck), France. Anhydrous ethanol (200 proof, ≥99.5%) was provided by Koptec (Decon Labs Inc., USA). As a typical example for preparing 10 g of SLM, Ga (7.5 g) and In (2.5 g) were mixed at a mass ratio of 75:25 in 20-ml disposable glass scintillation vials followed by thorough stirring. The mixture was heated in an oven at 70°C for 15 min to obtain the LM. Subsequently, 5 ml of anhydrous ethanol and 30 μl of hydrochloric acid (36.5 to 38%, Sigma-Aldrich, HX0603-3) were added, followed by sonication in an ice bath using a probe-type ultrasonic processor (Fangxu Scientific, 16NE2202) at 20 kHz and 30% amplitude in pulse mode (2-s ON/4-s OFF) for 3 min.

Separately, 0.2 g of SDBS was dissolved in 2 ml of deionized water using a bath-type ultrasonic cleaner (DK SONIC, DK-300PF) at 33 kHz and 120 W for 30 min. The resulting SDBS solution was added to the presonicated LM and subjected to a second round of sonication under the same conditions. The resulting suspension was transferred to a fume hood and dried at 80°C for 24 hours to yield SLM.

Characterizations and measurements

The conductivity of SLMs with varying compositions was evaluated using a standard four-point probe method. Contact angle measurements were conducted using a drop shape analyzer (KRÜSS, DSA30) inside a glovebox (Vigor, Ar atmosphere). Adhesion force between the LM and substrate was measured using a force gauge (MARK-10, M5-025). The structural, morphological, and compositional characterizations were carried out using field-emission SEM equipped with EDS (FE-SEM, Thermo Fisher Scientific, Apreo S).

Tensile and cyclic stretching tests were performed with GaIn, bGaIn, and SLM samples patterned on the VHB tape. The samples were subjected to uniaxial stretching using a universal testing machine (Jingkong, XLD-250E) at a strain rate of 150 mm min^{-1}, with the electrical resistance under strain recorded using an LCR meter (Hioki, IM3536-01). XRD patterns were obtained using an x-ray diffractometer (Malvern PANalytical, Empyrean Series 4). Raman spectra were recorded using a Raman spectrometer (HORIBA, LabRAM HR Evolution). Particle size distribution was measured by dynamic light scattering (Malvern, Zetasizer Nano ZS).

The width of the SLM traces was characterized by using an optical microscope (AmScope, FMA050). The 3D optical images of SLM trace were captured using a 3D digital microscope (Keyence, VHX-X1). All digital images were captured with a digital camera (Nikon, D7500). At least four samples were tested under each condition to ensure statistical reliability.

Design and fabrication of 3D shrinking electronics

To enable the fabrication of 3D circuits via localized NIR light absorption–induced folding, black ink patterns were initially designed using AutoCAD (2025) and printed onto PPS sheets (Cridoz, Shrinky Art Sheets) using a desktop laser printer (Brother, HL-L2380DW). For the fabrication of the 3D shrinkable ring, actual-size ring circuit pattern was designed in AutoCAD, scaled up by a factor of 2.5, and exported as DXF files for laser processing. A CO_2 laser machine (Universal Laser Systems, VLS2.3) was used to cut the polyimide (PI) tape (MEBMIK, MB-YCJ-0216-XJ4X20) uniformly

adhered to the smooth side of the PPS using 10% power and 15% speed settings. The excessive PI regions were peeled off using tweezers, with the exposed surface cleaned with ethanol-soaked cotton swabs, yielding the PI shadow mask with designed patterns.

Surface activation was performed using a plasma cleaner (Harrick Plasma, PDC-001-HP, air atmosphere) under medium intensity for 2 min to introduce hydrophilic functional groups. The SLM ink was applied to the patterned area using a blade and spread evenly using a soft paintbrush. Removing the PI shadow mask yielded the ring circuit before shrinkage, which was then heated in a furnace (Thermo Fisher Scientific, FB1315M) at 160°C for 10 min to induce shrinkage and form the miniaturized 3D ring circuit.

For electrical component integration, the soldering pads of the accelerometer module (ADXL345) and SMD resistors were first immersed in hydrochloric acid (36.5 to 38%, Sigma-Aldrich, HX0603-3) to remove surface oxides from the LM traces, ensuring electrical contact. After positioning the components onto the shrunk ring circuit, rapid local heating using a heat gun (Mypovos, 8588D) transformed the circuit onto the target 3D surface. The fabrication process for 3D conformal antennas was similar to that of the 3D ring, except without the integration of active components.

Simulation

Finite element analysis was conducted in Abaqus CAE (2022) to simulate the mechanical behavior and shrinkage of the PPS. Electromagnetic simulations of the antenna, including reflection coefficient (S_{11}), input impedance, current distribution, 3D radiation patterns, and E-/H-plane radiation patterns, were performed using the Antenna Designer toolbox in MATLAB (R2024a).

Application of the 3D shrinking electronics

Reflection coefficients of 3D conformal antennas were measured using a handheld vector network analyzer (SYSJOINT, NanoVNA-F V3), with the antenna bending angles controlled by the translation applied by a linear translation stage. The circuit layout of the 3D ring was designed using Altium Designer (24.0.1). The 1D-CNN model, t-SNE visualization, and game character control interface were all implemented in Python (3.11.9) within the Visual Studio Code environment.

Experiments on human subjects

All human subject studies were approved by The Pennsylvania State University (protocol number STUDY00020880), and informed consent was obtained from all volunteers.

Supplementary Materials

The PDF file includes:
Figs. S1 to S34
Tables S1 to S3
Legends for movies S1 to S5

Other Supplementary Material for this manuscript includes the following:
Movies S1 to S5

REFERENCES AND NOTES

1. X. Chen, W. Jian, Z. Wang, J. Ai, Y. Kang, P. Sun, Z. Wang, Y. Ma, H. Wang, Y. Chen, X. Feng, Wrap-like transfer printing for three-dimensional curvy electronics. *Sci. Adv.* **9**, eadi0357 (2023).
2. B. H. Kim, K. Li, J. T. Kim, Y. Park, H. Jang, X. Wang, Z. Xie, S. M. Won, H. J. Yoon, G. Lee, W. J. Jang, K. H. Lee, T. S. Chung, Y. H. Jung, S. Y. Heo, Y. Lee, J. Kim, T. Cai, Y. Kim, P. Prasopsukh, Y. Yu, X. Yu, R. Avila, H. Luan, H. Song, F. Zhu, Y. Zhao, L. Chen, S. H. Han, J. Kim, S. J. Oh, H. Lee, C. H. Lee, Y. Huang, L. P. Chamorro, Y. Zhang, J. A. Rogers, Three-dimensional electronic microfliers inspired by wind-dispersed seeds. *Nature* **597**, 503–510 (2021).
3. H. Song, G. Luo, Z. Ji, R. Bo, Z. Xue, D. Yan, F. Zhang, K. Bai, J. Liu, X. Cheng, W. Pang, Z. Shen, Y. Zhang, Highly-integrated, miniaturized, stretchable electronic systems based on stacked multilayer network materials. *Sci. Adv.* **8**, eabm3785 (2022).
4. Z. Xue, T. Jin, S. Xu, K. Bai, Q. He, F. Zhang, X. Cheng, Z. Ji, W. Pang, Z. Shen, H. Song, Y. Shuai, Y. Zhang, Assembly of complex 3D structures and electronics on curved surfaces. *Sci. Adv.* **8**, eabm6922 (2022).
5. B. Hou, D. Yang, X. Ren, L. Yi, X. Liu, A tactile oral pad based on carbon nanotubes for multimodal haptic interaction. *Nat. Electron.* **7**, 777–787 (2024).
6. Y. Luo, C. Liu, Y. J. Lee, J. DelPreto, K. Wu, M. Foshey, D. Rus, T. Palacios, Y. Li, A. Torralba, W. Matusik, Adaptive tactile interaction transfer via digitally embroidered smart gloves. *Nat. Commun.* **15**, 868 (2024).
7. C. Xu, Y. Song, J. R. Sempionatto, S. A. Solomon, Y. Yu, H. Y. Y. Nyein, R. Y. Tay, J. Li, W. Heng, J. Min, A. Lao, T. K. Hsiai, J. A. Sumner, W. Gao, A physicochemical-sensing electronic skin for stress response monitoring. *Nat. Electron.* **7**, 168–179 (2024).
8. H. Yoon, S. Jeong, B. Lee, Y. Hong, A site-selective integration strategy for microdevices on conformable substrates. *Nat. Electron.* **7**, 383–395 (2024).
9. B. Zhang, J. Li, J. Zhou, L. Chow, G. Zhao, Y. Huang, Z. Ma, Q. Zhang, Y. Yang, C. K. Yiu, J. Li, F. Chun, X. Huang, Y. Gao, P. Wu, S. Jia, H. Li, D. Li, Y. Liu, K. Yao, R. Shi, Z. Chen, B. L. Khoo, W. Yang, F. Wang, Z. Zheng, Z. Wang, X. Yu, A three-dimensional liquid diode for soft, integrated permeable electronics. *Nature* **628**, 84–92 (2024).
10. J. Zhou, J. Li, H. Jia, K. Yao, S. Jia, J. Li, G. Zhao, C. K. Yiu, Z. Gao, D. Li, B. Zhang, Y. Huang, Q. Zhuang, Y. Yang, X. Huang, M. Wu, Y. Liu, Y. Gao, H. Li, Y. Hu, R. Shi, M. Mukherji, Z. Zheng, X. Yu, Mormyroidea-inspired electronic skin for active non-contact three-dimensional tracking and sensing. *Nat. Commun.* **15**, 9875 (2024).
11. L. Yang, Z. Wang, H. Wang, B. Jin, C. Meng, X. Chen, R. Li, H. Wang, M. Xin, Z. Zhao, S. Guo, J. Wu, H. Cheng, Self-healing, reconfigurable, thermal-switching, transformative electronics for health monitoring. *Adv. Mater.* **35**, e2207742 (2023).
12. S. Zheng, X. Wang, W. Li, Z. Liu, Q. Li, F. Yan, Pressure-stamped stretchable electronics using a nanofibre membrane containing semi-embedded liquid metal particles. *Nat. Electron.* **7**, 576–585 (2024).
13. G. Li, M. Zhang, S. Liu, M. Yuan, J. Wu, M. Yu, L. Teng, Z. Xu, J. Guo, G. Li, Z. Liu, X. Ma, Three-dimensional flexible electronics using solidified liquid metal with regulated plasticity. *Nat. Electron.* **6**, 154–163 (2023).
14. K. Yao, Q. Zhuang, Q. Zhang, J. Zhou, C. K. Yiu, J. Zhang, D. Ye, Y. Yang, K. W. Wong, L. Chow, T. Huang, Y. Qiu, S. Jia, Z. Li, G. Zhao, H. Zhang, J. Zhu, X. Huang, J. Li, Y. Gao, H. Wang, J. Li, Y. Huang, D. Li, B. Zhang, J. Wang, Z. Chen, G. Guo, Z. Zheng, X. Yu, A fully integrated breathable haptic textile. *Sci. Adv.* **10**, eadq9575 (2024).
15. S. J. Woodman, D. S. Shah, M. Landesberg, A. Agrawala, R. Kramer-Bottiglio, Stretchable Arduinos embedded in soft robots. *Sci. Adv.* **9**, eadn6844 (2024).
16. N. Li, X. Yuan, Y. Li, G. Zhang, Q. Yang, Y. Zhou, M. Guo, J. Liu, Bioinspired liquid metal based soft humanoid robots. *Adv. Mater.* **36**, e2404330 (2024).
17. Y.-G. Park, H. S. An, J.-Y. Kim, J.-U. Park, High-resolution, reconfigurable printing of liquid metals with three-dimensional structures. *Sci. Adv.* **5**, eaaw2844 (2019).
18. Y. Jiang, D. Ye, A. Li, B. Zhang, W. Han, X. Niu, M. Zeng, L. Guo, G. Zhang, Z. Yin, Y. Huang, Transient charge-driven 3D conformal printing via pulsed-plasma impingement. *Proc. Natl. Acad. Sci. U.S.A.* **121**, e2402135121 (2024).
19. L. Zhang, X. Huang, T. Cole, H. Lu, J. Hang, W. Li, S. Y. Tang, C. Boyer, T. P. Davis, R. Qiao, 3D-printed liquid metal polymer composites as NIR-responsive 4D printing soft robot. *Nat. Commun.* **14**, 7815 (2023).
20. Y. Jo, H. J. Park, Y. B. Kim, S. S. Lee, S. Y. Lee, S. K. Kim, Y. Choi, S. Jeong, Form-factor free 3D copper circuits by surface-conformal direct printing and laser writing. *Adv. Funct. Mater.* **30**, 2004659 (2020).
21. T. Pinheiro, M. Morais, S. Silvestre, E. Carlos, J. Coelho, H. V. Almeida, P. Barquinha, E. Fortunato, R. Martins, Direct laser writing: From materials synthesis and conversion to electronic device processing. *Adv. Mater.* **36**, e2402014 (2024).
22. K. K. Kim, J. Choi, J. H. Kim, S. Nam, S. H. Ko, Evolvable skin electronics by in situ and in operando adaptation. *Adv. Funct. Mater.* **32**, 2106329 (2021).
23. K. Sim, S. Chen, Z. Li, Z. Rao, J. Liu, Y. Lu, S. Jang, F. Ershad, J. Chen, J. Xiao, C. Yu, Three-dimensional curvy electronics created using conformal additive stamp printing. *Nat. Electron.* **2**, 471–479 (2019).
24. C. Wang, C. Linghu, S. Nie, C. Li, Q. Lei, X. Tao, Y. Zeng, Y. Du, S. Zhang, K. Yu, H. Jin, W. Chen, J. Song, Programmable and scalable transfer printing with high reliability and efficiency for flexible inorganic electronics. *Sci. Adv.* **6**, eabb2393 (2020).
25. X. Huang, L. Liu, Y. H. Lin, R. Feng, Y. Shen, Y. Chang, H. Zhao, High-stretchability and low-hysteresis strain sensors using origami-inspired 3D mesostructures. *Sci. Adv.* **9**, eadh9799 (2023).
26. J. T. Overvelde, T. A. de Jong, Y. Shevchenko, S. A. Becerra, G. M. Whitesides, J. C. Weaver, C. Hoberman, K. Bertoldi, A three-dimensional actuated origami-inspired transformable metamaterial with multiple degrees of freedom. *Nat. Commun.* **7**, 10929 (2016).

27. Y. Zhang, C. Liu, B. Jia, D. Ma, X. Tian, Y. Cui, Y. Deng, Kirigami-inspired, three-dimensional piezoelectric pressure sensors assembled by compressive buckling. *npj Flex. Electron.* **8**, 23 (2024).
28. J. Choi, C. Han, S. Cho, K. Kim, J. Ahn, D. Del Orbe, I. Cho, Z.-J. Zhao, Y. S. Oh, H. Hong, S. S. Kim, I. Park, Customizable, conformal, and stretchable 3D electronics via predistorted pattern generation and thermoforming. *Sci. Adv.* **7**, eabj0694 (2021).
29. M. Kshitij, M. K. Dhal, A. Banerjee, V. Prasannavenkadesan, V. Katiyar, A. Kumar, Thermoplastic starch based melt processed films for packaging applications: Experimental and computational studies. *Mater Today Commun* **42**, 111475 (2025).
30. Y. Wu, C. Liu, M. Lapiere, J. L. Ciatti, D. S. Yang, J. Berkovich, J. B. Model, A. Banks, R. Ghaffari, J. K. Chang, R. G. Nuzzo, J. A. Rogers, Thermoplastic elastomers for wireless, skin-interfaced electronic, and microfluidic devices. *Adv. Mater. Technol.* **8**, 2300732 (2023).
31. M. Han, L. Chen, K. Aras, C. Liang, X. Chen, H. Zhao, K. Li, N. R. Faye, B. Sun, J. H. Kim, W. Bai, Q. Yang, Y. Ma, W. Lu, E. Song, J. M. Baek, Y. Lee, C. Liu, J. B. Model, G. Yang, R. Ghaffari, Y. Huang, I. R. Efimov, J. A. Rogers, Catheter-integrated soft multilayer electronic arrays for multiplexed sensing and actuation during cardiac surgery. *Nat. Biomed. Eng.* **4**, 997–1009 (2020).
32. H. Xu, W. Zheng, Y. Zhang, D. Zhao, L. Wang, Y. Zhao, W. Wang, Y. Yuan, J. Zhang, Z. Huo, Y. Wang, N. Zhao, Y. Qin, K. Liu, R. Xi, G. Chen, H. Zhang, C. Tang, J. Yan, Q. Ge, H. Cheng, Y. Lu, L. Gao, A fully integrated, standalone stretchable device platform with in-sensor adaptive machine learning for rehabilitation. *Nat. Commun.* **14**, 7769 (2023).
33. L. Xu, S. R. Gutbrod, A. P. Bonifas, Y. Su, M. S. Sulkin, N. Lu, H. J. Chung, K. I. Jang, Z. Liu, M. Ying, C. Lu, R. C. Webb, J. S. Kim, J. I. Laughner, H. Cheng, Y. Liu, A. Ameen, J. W. Jeong, G. T. Kim, Y. Huang, I. R. Efimov, J. A. Rogers, 3D multifunctional integumentary membranes for spatiotemporal cardiac measurements and stimulation across the entire epicardium. *Nat. Commun.* **5**, 3329 (2014).
34. S. Lee, Y. Song, Y. Ko, Y. Ko, J. Ko, C. H. Kwon, J. Huh, S. W. Kim, B. Yeom, J. Cho, A metal-like conductive elastomer with a hierarchical wrinkled structure. *Adv. Mater.* **32**, e1906460 (2020).
35. S. I. Rich, S. Lee, K. Fukuda, T. Someya, Developing the nondevelopable: Creating curved-surface electronics from nonstretchable devices. *Adv. Mater.* **34**, e2106683 (2022).
36. X. Mi, L. Liu, S. Yang, P. Wu, W. Zhan, X. Ji, J. Liang, Ink formulation of functional nanowires with hyperbranched stabilizers for versatile printing of flexible electronics. *Nat. Commun.* **16**, 2590 (2025).
37. S. Hao, L. Meng, Q. Fu, F. Xu, J. Yang, Low-Temperature tolerance and conformal adhesion zwitterionic hydrogels as electronic skin for strain and temperature responsiveness. *Chem. Eng. J.* **431**, 133782 (2022).
38. Y. Ohm, C. Pan, M. J. Ford, X. Huang, J. Liao, C. Majidi, An electrically conductive silver–polyacrylamide–alginate hydrogel composite for soft electronics. *Nat. Electron.* **4**, 185–192 (2021).
39. G. Yang, Y. Hu, W. Guo, W. Lei, W. Liu, G. Guo, C. Geng, Y. Liu, H. Wu, Tunable hydrogel electronics for diagnosis of peripheral neuropathy. *Adv. Mater.* **36**, e2308831 (2024).
40. Y. Qi, T. Jin, K. Yuan, J. You, C. Shen, K. Xie, Chemically stable polypyrrole-modified liquid metal nanoparticles with the promising photothermal conversion capability. *J. Mater. Sci. Technol.* **127**, 144–152 (2022).
41. Y. Qi, C. Shen, Q. Hou, Z. Ren, T. Jin, K. Xie, A self-healing liquid metal anode for lithium-ion batteries. *J. Energy Chem.* **72**, 522–531 (2022).
42. S. Liu, D. S. Shah, R. Kramer-Bottiglio, Highly stretchable multilayer electronic circuits using biphasic gallium-indium. *Nat. Mater.* **20**, 851–858 (2021).
43. L. Yang, L. Guo, Z. Wang, C. Meng, J. Wu, X. Chen, A. A. Musa, X. Jiang, H. Cheng, Stretchable triboelectric nanogenerator based on liquid metal with varying phases. *Adv. Sci.* **11**, e2405792 (2024).
44. W. He, X. Ye, T. Cui, Progress of shrink polymer micro- and nanomanufacturing. *Microsyst. Nanoeng.* **7**, 88 (2021).
45. Q. Li, C. Ding, W. Yuan, R. Xie, X. Zhou, Y. Zhao, M. Yu, Z. Yang, J. Sun, Q. Tian, F. Han, H. Li, X. Deng, G. Li, Z. Liu, Highly stretchable and permeable conductors based on shrinkable electrospun fiber mats. *Adv. Fiber Mater.* **3**, 302–311 (2021).
46. L. Tian, S. Khan, A. Shakeri, K. Jackson, A. T. Saif, F. Bayat, L. He, J. Gu, Y. Li, T. F. Didar, Z. Hosseinidoust, Virus-assembled biofunctional microarrays with hierarchical 3D nano-reticular network. *Adv. Funct. Mater.* **35**, 2414375 (2024).
47. A. Gupta, N. Al-Shamery, J. Lv, G. Thangavel, J. Park, D. Mandler, P. S. Lee, Stretchable energy storage with eutectic gallium indium alloy. *Adv. Energy Mater.* **15**, 2403760 (2024).
48. W. Xie, F. M. Allioux, R. Namivandi-Zangeneh, M. B. Ghasemian, J. Han, M. A. Rahim, J. Tang, J. Yang, M. Mousavi, M. Mayyas, Z. Cao, F. Centurion, M. J. Christoe, C. Zhang, Y. Wang, S. Merhebi, M. Baharfar, G. Ng, D. Esrafilzadeh, C. Boyer, K. Kalantar-Zadeh, Polydopamine shell as a Ga^{3+} reservoir for triggering gallium-indium phase separation in eutectic gallium-indium nanoalloys. *ACS Nano* **15**, 16839–16850 (2021).
49. N. A. Nor-Azman, M. B. Ghasemian, R. Fuchs, L. Liu, M. S. Widjajana, R. Yu, S. H. Chiu, S. A. Idrus-Saidi, N. Flores, Y. Chi, J. Tang, K. Kalantar-Zadeh, Mechanism behind the controlled generation of liquid metal nanoparticles by mechanical agitation. *ACS Nano* **18**, 11139–11152 (2024).
50. A. Yamaguchi, Y. Mashima, T. Iyoda, Reversible size control of liquid-metal nanoparticles under ultrasonication. *Angew. Chem. Int. Ed. Engl.* **54**, 12809–12813 (2015).
51. Y. Lin, J. Genzer, M. D. J. A. S. Dickey, Attributes, fabrication, and applications of gallium-based liquid metal particles. *Adv. Sci.* **7**, 2000192 (2020).
52. B. Yao, X. Xu, H. Li, Z. Han, J. Hao, G. Yang, Z. Xie, Y. Chen, W. Liu, Q. Wang, H. Wang, Soft liquid-metal/elastomer foam with compression-adjustable thermal conductivity and electromagnetic interference shielding. *Chem. Eng. J.* **410**, 128288 (2021).
53. B. B. Oliveira, A. R. Fernandes, P. V. Baptista, Shrinking cancer research barriers: Crafting accessible tumor-on-chip device for gene silencing assays. *Adv. Eng. Mater.* **26**, 2402254 (2024).
54. Z. Yan, F. Zhang, J. Wang, F. Liu, X. Guo, K. Nan, Q. Lin, M. Gao, D. Xiao, Y. Shi, Y. Qiu, H. Luan, J. H. Kim, Y. Wang, H. Luo, M. Han, Y. Huang, Y. Zhang, J. A. Rogers, Controlled mechanical buckling for origami-inspired construction of 3D microstructures in advanced materials. *Adv. Funct. Mater.* **26**, 2629–2639 (2016).
55. Y. Hou, Z. Li, Z. Wang, X. Zhang, Y. Li, C. Li, H. Guo, H. Yu, Programmable and surface-conformable origami design for thermoelectric devices. *Adv. Sci.* **11**, e2309052 (2024).
56. S. J. Wu, H. Yuk, J. Wu, C. S. Nabzdyk, X. Zhao, A multifunctional origami patch for minimally invasive tissue sealing. *Adv. Mater.* **33**, e2007667 (2021).
57. S. Liu, J. He, Y. Rao, Z. Dai, H. Ye, J. C. Tanir, Y. Li, N. Lu, Conformability of flexible sheets on spherical surfaces. *Sci. Adv.* **9**, eadf2709 (2023).
58. Y. Hong, Y. Chi, S. Wu, Y. Li, Y. Zhu, J. Yin, Boundary curvature guided programmable shape-morphing kirigami sheets. *Nat. Commun.* **13**, 530 (2022).
59. Q. Liu, W. Wang, H. Sinhmar, I. Griniasty, J. Z. Kim, J. T. Pelster, P. Chaudhari, M. F. Reynolds, M. C. Cao, D. A. Muller, A. B. Apsel, N. L. Abbott, H. Kress-Gazit, P. L. McEuen, I. Cohen, Electronically configurable microscopic metasheet robots. *Nat. Mater.* **24**, 109–115 (2025).
60. Z. Tian, B. Xu, G. Wan, X. Han, Z. Di, Z. Chen, Y. Mei, Gaussian-preserved, non-volatile shape morphing in three-dimensional microstructures for dual-functional electronic devices. *Nat. Commun.* **12**, 509 (2021).
61. M. Bhattacharjee, F. Nikbakhtnasrabadi, R. Dahiya, Printed chipless antenna as flexible temperature sensor. *IEEE Internet Things J.* **8**, 5101–5110 (2021).
62. H. Xu, W. Zheng, Y. Yuan, D. Xu, Y. Qin, N. Zhao, Q. Duan, Y. Jin, Y. Wang, W. Wang, Y. Lu, L. Gao, Flexible gas-permeable and resilient bowtie antenna for tensile strain and temperature sensing. *IEEE Internet Things J.* **9**, 23215–23223 (2022).
63. A. Karmakar, Fractal antennas and arrays: A review and recent developments. *Int. J. Microw. Wirel. Technol.* **13**, 173–197 (2020).
64. S. Chen, H.-Z. Wang, R.-Q. Zhao, W. Rao, J. Liu, Liquid metal composites. *Matter* **2**, 1446–1480 (2020).
65. J. Ma, F. Krisnadi, M. H. Vong, M. Kong, O. M. Awartani, M. D. Dickey, Shaping a soft future: Patterning liquid metals. *Adv. Mater.* **35**, e2205196 (2023).
66. N. Matsuhisa, M. Kaltenbrunner, T. Yokota, H. Jinno, K. Kuribara, T. Sekitani, T. Someya, Printable elastic conductors with a high conductivity for electronic textile applications. *Nat. Commun.* **6**, 7461 (2015).
67. N. Matsuhisa, D. Inoue, P. Zalar, H. Jin, Y. Matsuba, A. Itoh, T. Yokota, D. Hashizume, T. Someya, Printable elastic conductors by in situ formation of silver nanoparticles from silver flakes. *Nat. Mater.* **16**, 834–840 (2017).
68. P. Tan, H. Wang, F. Xiao, X. Lu, W. Shang, X. Deng, H. Song, Z. Xu, J. Cao, T. Gan, B. Wang, X. Zhou, Solution-processable, soft, self-adhesive, and conductive polymer composites for soft electronics. *Nat. Commun.* **13**, 358 (2022).
69. L. Zhang, K. S. Kumar, H. He, C. J. Cai, X. He, H. Gao, S. Yue, C. Li, R. C. Seet, H. Ren, J. Ouyang, Fully organic compliant dry electrodes self-adhesive to skin for long-term motion-robust epidermal biopotential monitoring. *Nat. Commun.* **11**, 4683 (2020).
70. H. Yuk, B. Lu, S. Lin, K. Qu, J. Xu, J. Luo, X. Zhao, 3D printing of conducting polymers. *Nat. Commun.* **11**, 1604 (2020).
71. L. Li, J. Meng, X. Bao, Y. Huang, X. P. Yan, H. L. Qian, C. Zhang, T. Liu, Direct-ink-write 3D printing of programmable micro-supercapacitors from MXene-regulating conducting polymer inks. *Adv. Energy Mater.* **13**, 2203683 (2023).
72. C. Arndt, M. Hauck, I. Wacker, B. Zeller-Plumhoff, F. Rasch, M. Taale, A. S. Nia, X. Feng, R. Adelung, R. R. Schroder, F. Schutt, C. Selhuber-Unkel, Microengineered hollow graphene tube systems generate conductive hydrogels with extremely low filler concentration. *Nano Lett.* **21**, 3690–3697 (2021).
73. J. Liu, L. McKeon, J. Garcia, S. Pinilla, S. Barwich, M. Mobius, P. Stamenov, J. N. Coleman, V. Nicolosi, Additive manufacturing of Ti_3C_2-MXene-functionalized conductive polymer hydrogels for electromagnetic-interference shielding. *Adv. Mater.* **34**, e2106253 (2022).
74. C. Tondera, T. F. Akbar, A. K. Thomas, W. Lin, C. Werner, V. Busskamp, Y. Zhang, I. R. Minev, Highly conductive, stretchable, and cell-adhesive hydrogel by nanoclay doping. *Small* **15**, e1901406 (2019).
75. Z. Chen, D. Zhao, B. Liu, G. Nian, X. Li, J. Yin, S. Qu, W. Yang, 3D printing of multifunctional hydrogels. *Adv. Funct. Mater.* **29**, 1900971 (2019).
76. Q. Ge, Z. Chen, J. Cheng, B. Zhang, Y.-F. Zhang, H. Li, X. He, C. Yuan, J. Liu, S. Magdassi, S. Qu, 3D printing of highly stretchable hydrogel with diverse UV curable polymers. *Sci. Adv.* **7**, eaba4261 (2021).

77. X. Luo, R. Wan, Z. Zhang, M. Song, L. Yan, J. Xu, H. Yang, B. Lu, 3D-printed hydrogel-based flexible electrochromic device for wearable displays. *Adv. Sci.* **11**, e2404679 (2024).
78. W. Lee, H. Kim, I. Kang, H. Park, J. Jung, H. Lee, H. Park, J. S. Park, J. M. Yuk, S. Ryu, J.-W. Jeong, J. Kang, Universal assembly of liquid metal particles in polymers enables elastic printed circuit board. *Science* **378**, 637–641 (2022).
79. R. Zhao, R. Guo, X. Xu, J. Liu, A fast and cost-effective transfer printing of liquid metal inks for three-dimensional wiring in flexible electronics. *ACS Appl. Mater. Interfaces* **12**, 36723–36730 (2020).

Acknowledgments: Y.Y. thanks R. Liu and S. Jiang for helpful discussions and insightful suggestions during the preparation of this manuscript. Y.Y. also acknowledges the support of the 2024–25 Vice Provost and Dean of the Graduate School Student Persistence Scholarship, provided by the J. Jeffrey and Ann Marie Fox Graduate School. **Funding:** H.C. acknowledges the support provided by NIH (award nos. U01DA056242 and R21EB030140), NSF (grant nos. 2309323, 2319139, and 2243979), and Penn State University. F.S. thanks the support from the National Science Foundation under grant no. 2239690. **Author contributions:** Conceptualization: H.C., Y.Y., and F.S. Methodology: Y.Y., H.C., D.C., and J.L. Software: Y.Y. and W.Z. Validation: Y.Y., H.C., J.L., W.Z., and M.A.A. Formal analysis: Y.Y., H.C., and W.Z. Investigation: Y.Y., H.C., B.L., W.Z., X.Z., A.M.A., A.D., F.T.Z., X.X., and M.A.A. Resources: H.C., F.S., and B.L. Data curation: Y.Y., H.C., and W.Z. Writing–original draft: Y.Y. Writing–review and editing: H.C., Y.Y., F.S., and D.C. Visualization: Y.Y. and B.L. Supervision: H.C. and Y.Y. Project administration: H.C. and F.S. Funding acquisition: H.C. and Y.Y. **Competing interests:** H.C. and Y.Y. are inventors on a provisional patent application related to this work (U.S. Provisional Patent Application No. 63/862,179). The other authors declare that they have no competing interests. **Data and materials availability:** All data needed to evaluate the conclusions in the paper are present in the paper and/or the Supplementary Materials.

Submitted 23 July 2025
Accepted 8 September 2025
Published 8 October 2025
10.1126/sciadv.aea8051